Supplement of Hydrol. Earth Syst. Sci., 30, 945–963, 2026
https://doi.org/10.5194/hess-30-945-2026-supplement

Hydrology and Earth System Sciences
Open Access
EGU

Supplement of

Hotspots and hot moments of metal mobilization: dynamic connectivity in legacy mine waters

Anita Alexandra Sanchez et al.

Correspondence to: Anita Alexandra Sanchez (anita.sanchez@mineral.tu-freiberg.de)

Contents

Section S1. Supplementary Information on methodology

Hydrological data collection and analysis. Water level loggers (Levelogger 5, Solinst Canada Ltd.) were installed at sites 1, 2, 3A, and 3B, where the water level and flow could be continuously monitored and quantified. The water level loggers at levels 1 and 2 recorded measurements from March 2022 to approximately January 2024 and the loggers at levels 3A and 3B recorded measurements from February 2022 to March 2024. The "Levelogger Software 4.6.2" was used to retrieve the recorded data. For precise measurement of water levels and flow at the outflow points of sites 1 and 2, plastic weirs were constructed and installed. Conversely, sites 3A and 3B were equipped with small spillways instead of weirs. The measurements obtained were critical for establishing the relationships between water levels and discharge rates. From Henderson (1996), the formula for triangular measuring weirs was used:

$$Q = \frac{8}{15} * C_d * \sqrt[2]{2 * g} * tan\left(\frac{\alpha}{2}\right) * h^{\frac{5}{2}} \qquad (S1)$$

where Q is the flow rate (in m^3/s], C_d is the discharge coefficient, g is the gravitational constant (9.81 m/s^2), α is the angle of the lower weir edge (°C) and h is the water level above the outlet (m). The water level-discharge relationship was applied at sites 1, 2, 3A, and 3B. A non-linear regression was used to transfer the data and using the Savitzky-Golay filter, the flows were correctly processed. Using the flow rate data, we identified different flow phases by observing flow rate patterns for each site and assigned each flow phase to a certain date range.

The stable isotopic composition of δ^2H and $\delta^{18}O$ were measured using cavity ring-down spectroscopy. Reference materials were measured as standards at the beginning of the measurements. All mine water samples collected at the four sites were measured eight times. The first three measurements were discarded, and the remaining measurements were weighted according to their position and using a hyperbolic fit. The hyperbolic values of the measurements were corrected using the standard values. Manual calibrations were continuously performed. From the δ^2H and $\delta^{18}O$ isotope data of surface precipitation, the LMWL was created. The LMWL indicates the regional meteoric influences on isotopic fractionation and is compared with the isotopic composition of the global precipitation using the GMWL formula (Craig, 1961):

$$\delta\,^2H = 8 * \delta^{18}O + 10 \qquad (S2)$$

The LMWL served as a reference for mine water samples to determine the origin of the mine water and variability of the samples collected. Several samples may be more strongly influenced by precipitation, or their isotopic composition may be more similar to "old" water or "young" water entering the mine.

Spectral processing and cubist model calibration. Chemometric models were calibrated from UV-Vis scans (i.e, measurements from the online UV-Vis spectrometer device, referred to as spectrolyzer here on) and corresponding analytical data (i.e., measurements from the Autosampler) to predict trace element concentrations.

UV-Vis spectra were recorded from 200 to 720 nm at a resolution of 0.5 nm. Raw spectra were cleaned by removing implausible scans (absorbance < 0 or absorbance > 4.5). Spectra were processed using the prospectr package Stevens and Ramirez-Lopez (2022). First, spectra were smoothed using a Savitzky Golay filter with a polynomial degree of 3 and a window size of 11 to remove noise. Then, a Standard Normal Variate (SNV) correction was applied. Both raw, smoothed and smoothed + snv-corrected spectra were used for model calibration.

Chemometric models were calibrated using the Cubist package Kuhn and Quinlan (2023) in the caret framework Kuhn (2008) for the following dissolved metal(loid)s: Mn, Ni, As, Cd, Pb, Fe, Al, Cu, and Zn. Models were calibrated both for untransformed and log1p-transformed variables, and using the three differently processed spectral sets (raw, smoothed, smoothed+snv). Cubist models were tuned for 1, 2, 5, 10, 20, and 50 committees and 0-9 neighbors using a 10-fold cross-validation. 75 % of the dataset was used for calibration and 25 % was held back for testing. The dataset was split using random, percentile-binned sampling. Model accuracy was evaluated using the test set, using a modified version of the evaluate_model() function found in the simplerspec package Baumann (2020) to calculate RMSE, R2, RPD, and Lin's concordance correlation coefficient among other valuation statistics. An example for the predictions for the test set can be seen in section S4.

Hysteresis analysis. To capture dynamic transport mechanisms, hysteresis behavior in C-Q relationships was also evaluated using hysteresis index (HI) methods developed by Lloyd et al. (2016), Zuecco et al. (2016), and Harp et al. (2023). Hysteresis patterns reveal time lags between discharge and concentration, offering insights into hydraulic connectivity (Pohle et al., 2021) and mobilization processes at large (Lloyd et al., 2016). The Lloyd index compares normalized changes in concentration and discharge across an event, defined as:

$$HI = (C_{rise} - C_{fall}) / C_{mid} \quad (S3)$$

where C_{rise} is the concentration on the rising limb at a given percentile of discharge, C_{fall} is the concentration on the falling limb at the same percentile of discharge, and C_{mid} is the median concentration during the whole event, used for normalization. The final HI is used as a mean for all percentile-step hysteresis values.

The Zuecco index applies an angle-based approach in C-Q space that calculates the integrated area between rising and falling limbs:

$$HI = M * sin\left(\theta - \frac{\pi}{4}\right) \quad (S4)$$

where $\theta = arctan(\frac{\Delta C}{\Delta Q})$ is the angle of the C-Q vector segment, $M = \sqrt{(\Delta Q)^2 + (\Delta C)^2}$ is the vector magnitude, and ΔQ and ΔC are incremental changes in discharge and concentration, respectively. This formula accounts for both loop direction and strength. The Zuecco index results in a 9-class classification index, with classes 1-4 being clockwise variants, 5-8 being counterclockwise variants, and class 0 being no hysteresis.

These approaches quantify the direction and magnitude of hysteresis loops observed across different phases. Clockwise hysteresis reflects higher concentrations on the rising limb, suggesting rapid mobilization and proximity of hydrogeochemical sources, whereas counterclockwise hysteresis occurs when concentrations on the falling limb exceed those on the rising limb, indicating that high concentration sources are distant from the sampling location (Pohle et al., 2021).

In both approaches, HI values typically range from -1 to +1, with positive values indicating clockwise hysteresis and negative values indicating counterclockwise hysteresis (Vaughan et al., 2017). The meaning of hysteresis typically depends on whether C-Q behavior shows enrichment or dilution, and clockwise/counterclockwise loops are interpreted in combination with slope and event context.

We additionally applied the HARP (Hysteresis Area, Residual, and Peaks) metrics of Roberts et al. (2023), which characterize event structure even in cases where traditional HI methods return near-zero values for complex loops. The empirical classification is based on peak timing difference between Q and C, loop shape and area, and residual (end of state deviation). HARP defines four key metrics based on min-max normalized C-Q curves:

1. Hysteresis Area

$$A = \int_Q C(Q)\, dQ, \qquad A = \in [0, \pm 1] \quad (S5)$$

The area enclosed by the loop is calculated using numerical integration. This metric measures the degree and direction of hysteresis in the C-Q relationship. A = 0 corresponds to an event without hysteresis. Larger magnitudes reflect greater difference between the concentrations on the rising and falling limbs. The sign indicates clockwise (+) or counterclockwise (-) dominance.

2. Residual

$$R = C_f(0) - C_r(0) \quad (S6)$$

The difference in concentration between the rising and falling limbs at Q = 0.

3. Peak discharge

$$\hat{Q} = T|(Q = 1) \quad (S7)$$

The percentage of time into the event that the peak discharge is observed.

4. Peak concentration

$$\hat{C} = T|(C = 1) \quad (S8)$$

The percentage of time into the event that the peak concentration is observed.

These HARP metrics reveal event-scale solute dynamics including source proximity, mixing regimes, and hydrogeochemical memory (Roberts et al., 2023). Together, the three approaches provide a comprehensive framework for identifying shifts in contaminant availability, transport timing, and hydrological connectivity across the mine system.

Section S2. Supplementary Information on characteristics of sampled locations

Reiche Zeche mine. Selected physicochemical parameters of sites sampled in Reiche Zeche collected for the entire two-year sampling period in all three levels and the central drainage adit were obtained. These parameters included: pH, Electrical Conductivity (EC), Dissolved Organic Carbon (DOC), Dissolved Inorganic Carbon (DIC), and dissolved metal(loid) concentrations. All analyses were performed in the laboratory. The number of samples (n) obtained for each site were averaged (± standard error) and used as a comparison to highlight the quantitative differences between the four sites and are provided in **Table S1**.

Table S1. Average values and standard errors (SE) of physicochemical parameters of water sampling sites from several locations of Schwarzer Hirsch Stehender, Reiche Zeche. Standard error was calculated as SE = SD/√n, where SD is the standard deviation and n is the number of samples per site. NA refers to values being below the limit of detection.

	Site 1					Site 2					Site 3A					Site 3B				
Parameters	Mean	Min	Max	SE	n	Mean	Min	Max	SE	n	Mean	Min	Max	SE	n	Mean	Min	Max	SE	n
pH	5.5	3.7	6.4	0.09	32	3.5	3.0	4.1	0.05	37	3.1	2.9	3.7	0.03	34	3.3	2.9	3.9	0.05	37
EC(μs/cm)	320	290	549	7.65	32	552	328	1066	31.1	37	1097	545	2350	82.1	34	725	366	1396	44.6	37
Q (mL/s)	280	53.6	893	44.9	25	166	5.49	670	36.3	28	285	125	596	21.1	33	285	116	720	27.8	33

δ^2H	-60.0	-66.9	-49.7	0.50	32	-60.5	-67.0	-43.7	0.58	34	-61.6	-66.9	-59.9	0.23	33	-61.0	-65.1	-57.4	0.23	35
$\delta^{18}O$	-8.90	-10.1	-5.32	0.14	32	-8.95	-10.3	-3.13	0.19	34	-9.22	-10.4	-8.92	0.05	33	-9.09	-9.73	-8.56	0.05	35
DOC(mg/L)	1.2	0.73	1.9	0.05	32	1.3	0.86	2.3	0.06	37	1.8	0.66	8.1	0.24	34	1.5	0.85	7.2	0.17	37
DIC(mg/L)	0.71	0.00	2.0	0.06	32	0.33	0.00	0.90	0.03	37	0.40	0.00	1.1	0.04	34	0.30	0.00	0.96	0.03	37
Fe(mg/L)	0.02	0.003	0.26	0.008	32	3.7	0.08	23	0.97	37	3.3	0.27	8.1	0.27	34	2.4	0.29	9.2	0.32	37
Zn(mg/L)	1.6	1.3	2.3	0.05	32	14	2.7	49	1.8	37	106	14	477	21	34	28	4.3	75	3.2	37
Pb(mg/L)	0.06	0.009	0.16	0.006	32	1.0	0.23	1.8	0.08	37	0.90	0.42	1.6	0.06	34	1.2	0.3	2.0	0.08	37
Cd(mg/L)	0.013	0.007	0.025	0.001	32	0.13	0.025	0.42	0.02	37	0.83	0.24	3.3	0.14	34	0.27	0.030	0.74	0.03	37
Cu(mg/L)	0.018	0.002	0.037	0.001	32	0.35	0.063	1.26	0.05	37	1.6	0.35	4.0	0.16	34	0.70	0.12	2.0	0.07	37
Al(mg/L)	0.047	0.006	0.21	0.009	32	2.6	0.39	9.9	0.39	37	16	2.4	73	3.1	34	4.9	0.29	17	0.64	37
Mn(mg/L)	0.067	0.032	0.19	0.008	32	1.1	0.25	3.9	0.15	37	7.3	1.2	32	1.3	34	2.2	0.40	6.6	0.26	37
Ni(mg/L)	0.011	0.007	0.015	0.0003	32	0.022	0.01	0.04	0.001	37	0.070	0.019	0.24	0.009	34	0.030	0.011	0.066	0.002	37
As(mg/L)	NA	NA	NA	NA	32	0.11	0.10	0.23	0.005	37	NA	NA	NA	0.00	34	NA	NA	NA	NA	37

Section S3. Supplementary Information on spatial and temporal dynamics and trends

Dynamics of four sites compared to other sampling sites. The temporal trends of dissolved metals at sites 1, 2, 3A, and 3B were compared to other sites among the three levels within Reiche Zeche from February 2nd, 2022 to May 31st, 2024 (**Figure S1 a-i**). All four sites exhibit distinct episodic surges in dissolved Fe, Zn, Al, Cd, Pb, Cu, Mn, and Ni, with concentrations rising sharply and then returning to baseline levels. Sites 3A and 3B tend to have the largest accumulation of metal concentrations right before the occurrence of each flush phase, which then causes a great dilution of the present metals. These high-release events suggest that metal(loid) mobilization originates from material in contact with the deeper water layers rather than the surface outflow. The timing of these events appears seasonal, likely influenced by hydrological or biogeochemical triggers such as stratification development during low flow, breakdown during high flow or shifts in associated redox conditions. In contrast to the trends observed for the other metals, dissolved Pb concentrations remained relatively stable across all sites (except site 1), suggesting that Pb may be present in generally lower quantities at the deeper sites or that it is less susceptible to episodic mobilization under varying hydrological conditions. In addition, metal concentrations at the other sites among the RZ levels remain low and relatively stable over time.

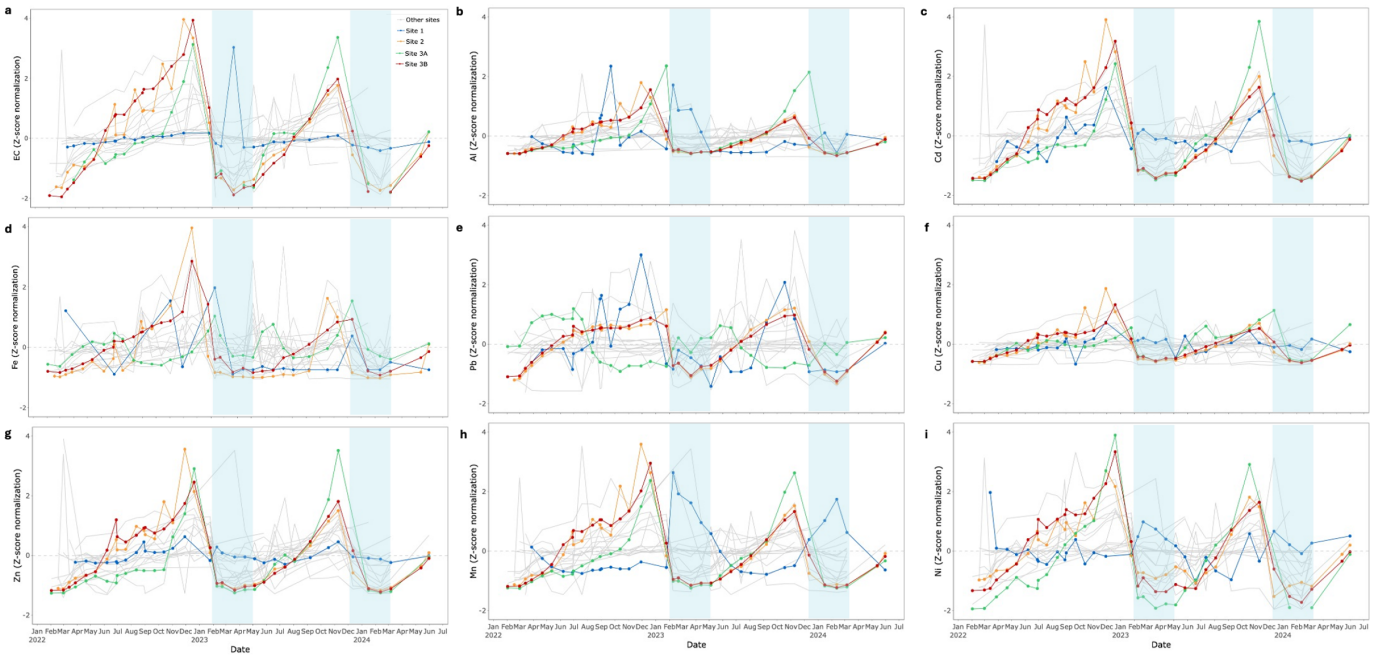

Figure S1: Spatial and temporal dynamics in (a) electrical conductivity, dissolved (b) Al, (c) Cd, (d) Fe, (e) Pb, (f) Cu, (g) Zn, (h) Mn, and (i) Ni concentrations across the mine system. Values are z-scaled, i.e. dissolved Al concentrations are visualized in standard deviations away from the site mean. Individual sites are connected by black lines and colored lines are monitored flow sites for sites 1, 2, 3A, and 3B. The blue panel highlights the year 1 and 2 flush period.

The spatial synchrony in geochemical responses across mine levels suggest a system-wide process of transient hydrological connectivity further shown through isotopic analyses of $\delta^{2}H$ and $\delta^{18}O$ (**Figure S2**). During low and declining flow phases, samples collected at all four sites exhibited stable isotopic signatures clustering near the Local Meteoric Water Line (LMWL), indicative of mixing with older, stored water. In contrast, during flush phases, isotopic compositions deviated from the background, trending toward more younger signatures. This shift suggests rapid mobilization of recent meteoric inputs along reactivated pathways (Spangenberg et al., 2007; Swenson et al., 2024). The similarity in isotopic patterns across years and sites reinforces the presence of a recurrent threshold-driven connectivity regime, wherein hydrological re-connectivity causes a pulse-like release of fresher water.

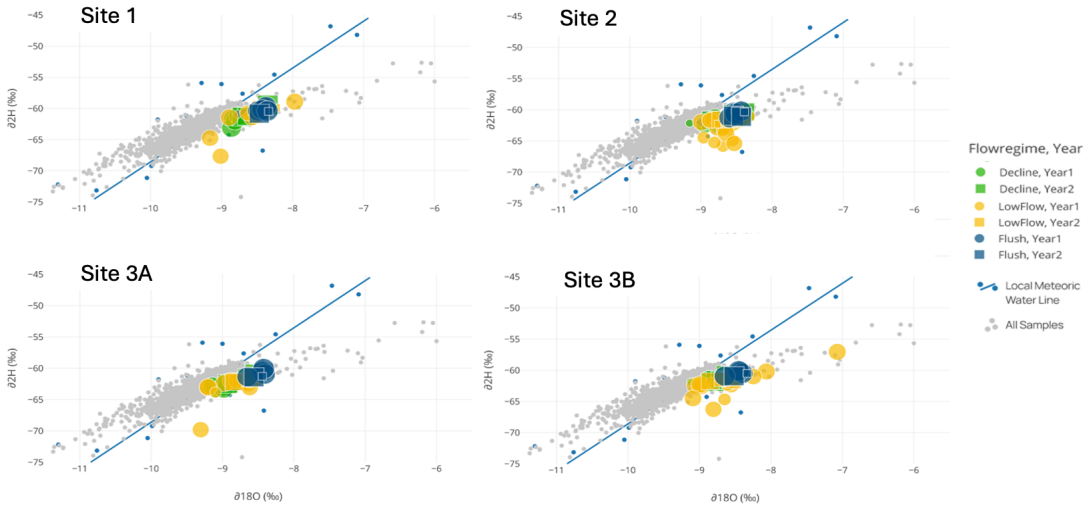

Figure S2: Isotope signatures of the water samples collected at sites (a) 1, (b) 2, (c) 3A, and (d) 3B are shown. The blue line presents the local meteoric water line. In the background, all samples from the project until March 2024 are shown in grey. Green markers present the declining flow phase, yellow markers display the low flow phase, and blue markers present the flush phase with marker shapes differentiating between the two years (circle - year 1; square - year 2).

Metal(loid) loads for each flow phase across two years. **Table S2** summarizes the quantity of dissolved metal(loid) loads (kg/day) across declining, low, and flush flow phases for sites 1, 2, 3A, and 3B during years 1 and 2. A clear pattern emerges where sites 2, 3A, and 3B consistently exhibited the highest total metal loads during low flow periods **(Figure S3)**, especially for Zn, Al, Fe, and Mn, indicating substantial mobilization from persistent, slowly accessed subsurface sources. In contrast, site 1 showed peak loads during the flush phase, consistent with shorter residence times and faster hydrological turnover. Zn dominated the load profile across all deeper sites, with year 1 values during low flow reaching over 30 kg/day at site 3A, underscoring its major role in overall contaminant flux. Notably, Cd loads remained relatively low across all sites, but their persistence across phases, particularly at sites 2 and 3B, supports the interpretation of diffuse and conservative transport behavior. Meanwhile, Pb, Cu, and Ni showed more variability between sites and years, with site 3A standing out as a potential hotspot in both years. Interannual differences were also evident. While site 2's total loads were similar between years, sites 3A and 3B displayed significantly higher values in year 1 for most metal(loid)s, particularly Zn and Al. These differences likely reflect greater system connectivity following drier periods at these deeper sites.

Table S2. Quantity of dissolved metal(loid) loads for year 1 and 2 of declining, low flow, and flush phases for each site. NA refers to metal(loid) loads not quantified due to insufficient discharge data or concentration values below the detection limit.

		Site 1			Site 2			Site 3A			Site 3B		
Metal(loid) load (kg/d)	Year	Declining Flow	Low Flow	Flush	Declining Flow	Low Flow	Flush	Declining Flow	Low Flow	Flush	Declining Flow	Low Flow	Flush
Fe	1	0.0003	0.003	0.005	0.050	0.295	0.099	0.368	0.790	0.649	0.106	0.751	0.213
Zn	1	0.125	0.200	0.381	0.293	1.150	0.856	4.703	30.791	4.256	1.273	8.233	1.633
Cd	1	0.0009	0.002	0.003	0.003	0.011	0.008	0.046	0.241	0.042	0.013	0.080	0.017
Pb	1	0.004	0.008	0.009	0.030	0.081	0.106	0.179	0.243	0.172	0.097	0.306	0.132
Cu	1	0.001	0.002	0.026	0.007	0.029	0.021	0.129	0.427	0.105	0.039	0.200	0.052
Al	1	0.003	0.006	0.026	0.046	0.229	0.113	0.751	4.767	0.687	0.203	1.553	0.261
Mn	1	0.006	0.005	0.034	0.021	0.094	0.066	0.353	2.247	0.332	0.102	0.664	0.135
Ni	1	0.001	0.001	0.003	0.0007	0.002	0.003	0.005	0.022	0.005	0.002	0.008	0.004
As	1	NA	NA	NA	NA	0.006	NA	NA	NA	NA	NA	NA	NA
Fe	2	0.001	0.0004	NA	0.013	0.058	0.017	0.291	0.224	0.239	0.092	0.074	0.186
Zn	2	0.168	0.070	NA	0.392	0.328	0.191	3.303	13.662	7.070	1.439	0.994	1.483
Cd	2	0.001	0.0006	NA	0.004	0.003	0.002	0.031	0.104	0.053	0.014	0.009	0.014
Pb	2	0.003	0.002	NA	0.044	0.028	0.025	0.089	0.046	0.045	0.113	0.044	0.078
Cu	2	0.002	0.0008	NA	0.009	0.008	0.005	0.092	0.194	0.079	0.044	0.024	0.040
Al	2	0.001	0.0008	NA	0.054	0.059	0.028	0.463	1.933	1.101	0.222	0.161	0.199
Mn	2	0.009	0.002	NA	0.026	0.025	0.013	0.222	0.859	0.480	0.107	0.069	0.106
Ni	2	0.001	0.0004	NA	0.001	0.0005	0.0002	0.003	0.008	0.004	0.002	0.0009	0.002
As	2	NA	NA	NA	NA	NA	NA	NA	NA	NA	NA	NA	NA

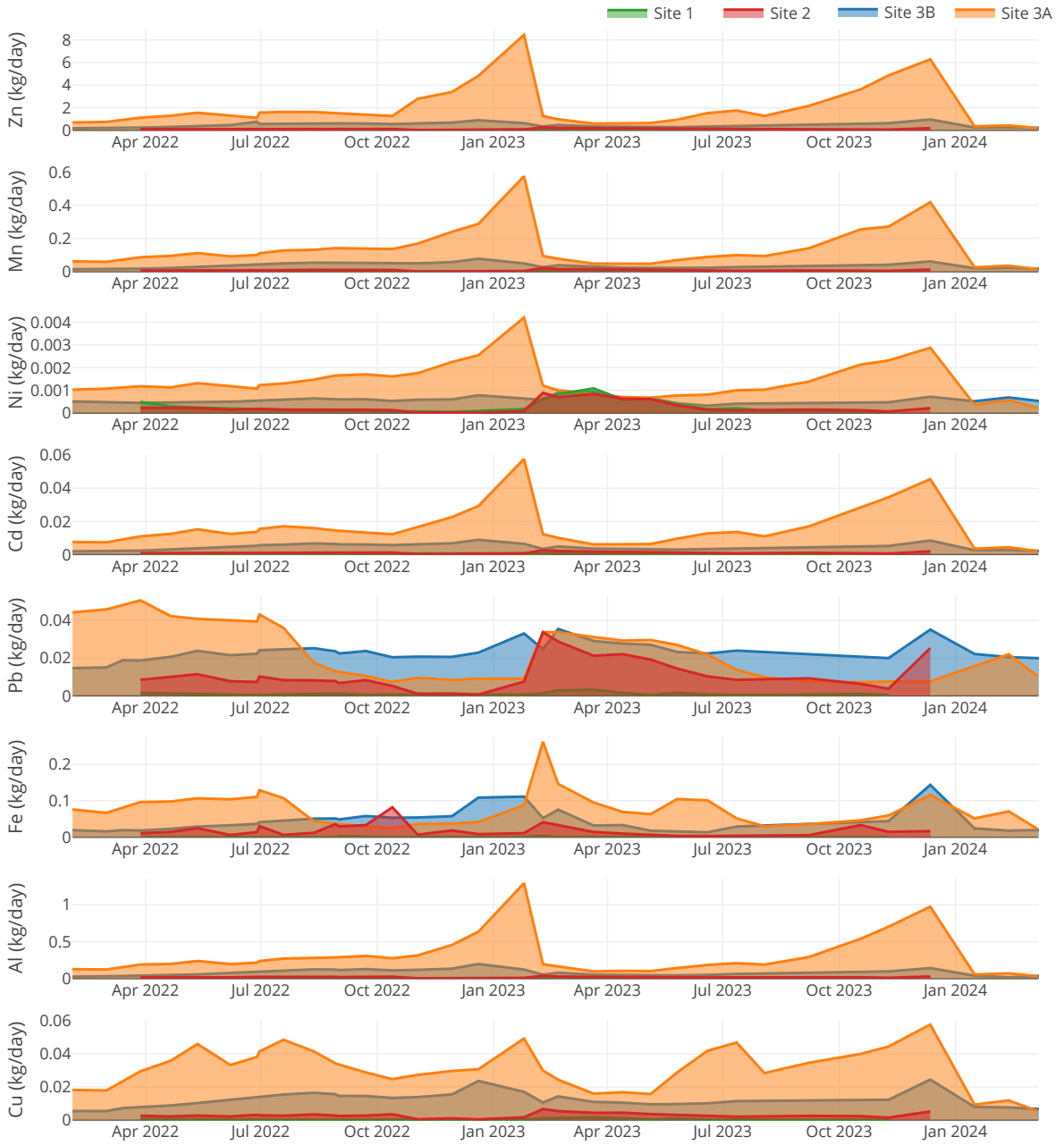

Figure S3. Metal(loid) loads from February 2022 to March 2024 are shown for sites 1, 2, 3A, and 3B. Arsenic is not shown since concentration values were generally below the detection limit.

Section S4. Supplementary Information on C-Q relationships

C-Q slopes across two years. The slope values from C-Q relationships (calculated from the entire sampling period) were compared among sites 1, 2, 3A, and 3B (**Table S3**). These slopes provide insight into solute mobilization behavior, ranging from dilution ($b < 0$), to enrichment ($b > 0$), to chemostatic ($b \approx 0$). Site 1 showed a wide variability across constituents, with several metals exhibiting near-zero or weakly positive slopes, indicating mixed chemostatic and enrichment behavior. In contrast, sites 2, 3A, and 3B displayed predominately dilution behavior across the entire sampling period, particularly for Zn, Al, and Mn. The strongest dilution slopes occurred at site 3A (e.g., Zn, b = -1.785; Al, b = -

1.662; Mn, b = -1.627) and site 3B (e.g., Zn, b = -1.580; Al, b = -1.820; Mn, b = -1.555). The strong negative slopes indicate source-limited mobilization, suggesting solute concentrations decline rapidly with increasing discharge due to flushing of stored contaminants. DOC, pH, and EC also followed consistent dilution trends at sites 2, 3A, and 3B, reinforcing the interpretation that increased flows reduce solute concentrations via dilution and mixing with low-concentration water. Together, these C–Q slope patterns reveal spatial and temporal differences in solute sourcing that align with transient flow path activation and fill-and-spill dynamics observed in the hysteresis analysis.

Table S3. Total number of constituent samples and concentration-discharge regression slopes (±SE) for four monitored flow sites. NA refers to concentration values below the detection limit. All C-Q slopes are in log_{10}-log_{10} space.

	Site 1		Site 2		Site 3A		Site 3B	
Parameter	Total samples (n)	C-Q slope (β)	Total samples (n)	C-Q slope (β)	Total samples (n)	C-Q slope (β)	Total samples (n)	C-Q slope (β)
Fe (mg/L)	23	-0.160 (±0.32)	28	-0.994 (±0.13)	33	-0.140 (±0.20)	33	-1.443 (±0.20)
Zn (mg/L)	25	-0.111 (±0.04)	28	-0.546 (±0.04)	33	-1.785 (±0.32)	33	-1.580 (±0.13)
Cd (mg/L)	25	-0.187 (±0.08)	28	-0.550 (±0.05)	33	-1.522 (±0.30)	33	-1.533 (±0.13)
Pb (mg/L)	25	-0.575 (±0.12)	28	-0.286 (±0.04)	33	0.687 (±0.15)	33	-0.932 (±0.09)
Cu (mg/L)	25	-0.070 (±0.15)	28	-0.555 (±0.05)	33	-1.156 (±0.23)	33	-1.367 (±0.11)
Al (mg/L)	25	0.113 (±0.28)	28	-0.672 (±0.06)	33	-1.662 (±0.32)	33	-1.820 (±0.15)
Mn (mg/L)	25	0.493 (±0.09)	28	-0.584 (±0.05)	33	-1.627 (±0.32)	33	-1.555 (±0.13)
Ni (mg/L)	25	0.082 (±0.04)	28	-0.249 (±0.03)	33	-1.238 (±0.25)	33	-0.875 (±0.08)
As (mg/L)	25	NA	28	-0.084 (±0.03)	33	NA	33	NA
DOC (mg/L)	25	0.055 (±0.06)	28	-0.109 (±0.04)	33	-0.789 (±0.22)	33	-0.398 (±0.12)
DIC (mg/L)	25	0.097 (±0.08)	27	0.023 (±0.06)	32	0.201 (±0.20)	32	-0.100 (±0.16)
H^+ (mol/L)	25	0.701 (±0.29)	28	-0.460 (±0.05)	33	-0.360 (±0.17)	33	-1.027 (±0.14)
EC (µs/cm)	25	0.0172 (±0.03)	28	-0.239 (±0.02)	33	-0.687 (±0.13)	33	-0.682 (±0.06)
PLI	25	0.0495 (±0.08)	28	-0.502 (±0.04)	33	-0.960 (±0.20)	33	-1.234 (±0.10)

Identification of geochemical phases. To support the development of the geochemical phase framework (Section 2.6.5 in main text), we examined the co-evolution of several hydrological and geochemical indicators over time at sites 1, 2, 3A, and 3B. Because no single metric could capture the complex transitions in contaminant mobilization, we relied on joint interpretation of trends in discharge, water availability index (i.e., wetness), pollution load index, C-Q slope, CV_c/CV_q ratio, and hysteresis index using methods from Zuecco et al. (2016), and Roberts et al. (2023; HARP area). Plotting these variables together allowed us to detect consistent temporal patterns, such as shifts from low flow and loading to flushing, dilution, and/or chemostatic, that were not fully visible from C-Q relationships alone. The **Figure S4** first shows the relationship between C-Q slope and CV_c/CV_q ratios, as well as the

relationship between changes in concentration versus changes in discharge, among all the sites using the PLI values. Then, the multi-parameter trends revealed the diagnostic signals that informed the automated classification of loading, flushing, dilution, recession, chemostatic, and variable-source phases.

Figure S4. Spread of geochemical phases from the C-Q analysis (PLI) showing (a) C-Q slope versus CV_c/CV_q ratio and (b) the change in concentration versus the change in discharge. Time series comparison of key hydrological and geochemical indicators used to identify geochemical phases at (c-

f) sites 1, 2, 3A, and 3B. Each panel shows scaled values of discharge (Q), pollution load index (PLI), C-Q slope, hysteresis index (HI) from Zuecco et al. (2016), hysteresis area from the HARP method from Roberts et al. (2023), and the water availability index (wetness). Interpreting these parameters jointly allowed identification of temporal transitions in solute behavior, including periods of loading, flushing, dilution, recession, chemostatic-like stability, and variable source conditions. These integrated trends formed the basis of geochemical phase classification described in Section 2.6.5 and illustrated the timing, magnitude, and co-evolution of hydrological and geochemical drivers controlling contaminant mobilization in the mine system.

Section S5. Supplementary Information on cubist modeling results

Cubist modeling. The performance and interpretive power of the Cubist regression modeling approach that was applied using the spectrolyzer data and autosampler data is illustrated in **Figure S5**. Figure S5 demonstrates strong agreement between measured and predicted concentrations of Zn, Fe, and Cd, with slope (b) and coefficient of determination (r^2) values indicating robust model performance, particularly for identifying peak events and transitions between flow regimes.

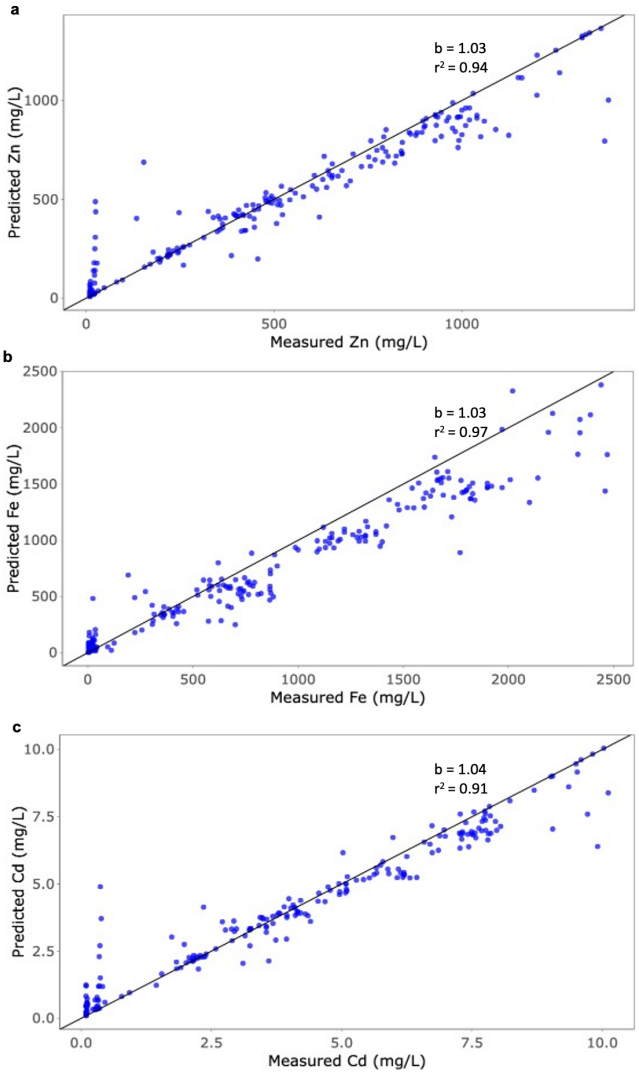

Figure S5. Measured (from the autosampler) versus predicted dissolved concentrations for (a) Zn, (b) Fe, and (c) Cd from cubist modeling results and goodness of fit line is shown. The calculated slope (b) and coefficient of determination (r^2) values are presented.

Section S6. Supplementary Information on visuals of sampling sites

Images of sites. Images were taken of all sampling sites throughout the over two-year sampling period. The images were taken sporadically and were predominately taken during periods of high flow, given that during low flow, the quantity of water was much less and the visuality of where water was collected at the sampling site was difficult to see. **Figure S6** displays images of the four sampling sites focused on in this study taken in February 2023.

Figure S6. Photos of sampling sites 1, 2, 3A, and 3B taken on February 9, 2023.

References

Baumann, P. (2020): simplerspec: soil and plant spectroscopic model building and prediction, available at: https://github.com/philipp-baumann/simplerspec, last access: 1 May 2025.

Craig, H.: Isotopic Variations in Meteoric Waters, Reinhold, 1934.

Henderson, F. M.: Open Channel Flow, MacMillan, New York, 1966.

Kuhn, M.: Building predictive models in R using the caret package, Journal of Statistical Software, 28, 1–26, https://doi.org/10.18637/jss.v028.i05, 2008.

Kuhn, M. and Quinlan, R. (2023): Cubist: rule- and instance-based regression modeling, available at: https://CRAN.R-project.org/package=Cubist, last access: 1 May 2025.

Lloyd, C. E. M., Freer, J. E., Johnes, P. J., and Collins, A. L.: Technical Note: Testing an improved index for analysing storm discharge–concentration hysteresis, Hydrol. Earth Syst. Sci., 20, 625–632, https://doi.org/10.5194/hess-20-625-2016, 2016.

Pohle, I., Baggaley, N., Palarea-Albaladejo, J., Stutter, M., and Glendell, M.: A Framework for Assessing Concentration-Discharge Catchment Behavior From Low-Frequency Water Quality Data, Water Resources Research, 57, https://doi.org/10.1029/2021wr029692, 2021.

Roberts, M. E., Kim, D., Lu, J., and Hamilton, D. P.: HARP: A suite of parameters to describe the hysteresis of streamflow and water quality constituents, J. Hydrol., 626, 130262, https://doi.org/10.1016/j.jhydrol.2023.130262, 2023.

Spangenberg, J. E., Dold, B., Vogt, M. L., and Pfeifer, H. R.: Stable hydrogen and oxygen isotope composition of waters from mine tailings in different climatic environments, Environmental Science and Technology, 41, 1870–1876, https://doi.org/10.1021/es061654w, 2007.

Stevens, A. and Ramirez-Lopez, L. (2022): An introduction to the prospectr package, available at: https://cran.r-project.org/web/packages/prospectr/index.html, last access: 1 May 2025.

Swenson, L. J., Zipper, S., Peterson, D. M., Jones, C. N., Burgin, A. J., Seybold, E., Kirk, M. F., and Hatley, C.: Changes in Water Age During Dry-Down of a Non-Perennial Stream, Water Resources Research, 60, https://doi.org/10.1029/2023wr034623, 2024.

Vaughan, M. C. H., Bowden, W. B., Shanley, J. B., Vermilyea, A., Sleeper, R., Gold, A. J., Pradhanang, S. M., Inamdar, S. P., Levia, D. F., Andres, A. S., Birgand, F., and Schroth, A. W.: High-frequency dissolved organic carbon and nitrate measurements reveal differences in storm hysteresis and loading in relation to land cover and seasonality, Water Resources Research, 53, 5345–5363, https://doi.org/10.1002/2017wr020491, 2017.

Zuecco, G., Penna, D., Borga, M., and Meerveld, H. J. van: A versatile index to characterize hysteresis between hydrological variables at the runoff event timescale, Hydrol. Process., 30, 1449–1466, https://doi.org/10.1002/hyp.10681, 2016.